# Development of Microstructural Damage in Ni-Based Alloys During Creep

MITSUHARU YONEMURA, HIROYUKI SEMBA, and MASAAKI IGARASHI

Ni-based model alloys with a base composition of Ni-20 mass pct Cr-3 mass pct Mo that were precipitation strengthened by the $\gamma'$ phase were studied in regards to their failure mechanisms as part of the fundamental research for achieving a creep rupture strength of 100 MPa at 1023 K (750 °C) and $10^5$ hours. The microstructure, which was interrupted by transient creep, as well as the minimum creep rate and accelerated creep at 1123 K (850 °C) and 80 MPa was observed. The microstructure around the grain boundaries was altered remarkably with strain-induced grain boundary migration, while the $\gamma'$ particle size increased linearly inside the grains with increasing temperature and time. Furthermore, the volume fraction of the $\gamma'$ phase and the amount of precipitation on the grain boundary were associated with the size of the precipitate-free zone (PFZ), which is a major factor in creep damage. The appropriate precipitations inside the grains and at the grain boundaries were very effective for suppressing PFZ. Consequently, the creep properties can be improved by controlling PFZ in the proximity of grain boundaries for a superior balance of creep strength and ductility.

## I. INTRODUCTION

ALLOYING optimization studies of steels and alloys that can be used in advanced ultra-super critical (A-USC) power plants which operated at a steam condition of at least 1023 K (700 °C) and 35 MPa were conducted along with fundamental investigations into creep degradation and failure mechanisms in order to obtain an alloy design guideline for heat-resistant steels and alloys for boiler tubes.[1]

In Ni-based superalloys, it is not difficult to maintain creep strength at high temperatures due to precipitation hardening of the coherent $\gamma'$-Ni$_3$Al phase to the FCC-$\gamma$ matrix. Many groups have studied the morphological changes of $\gamma'$ particles,[2] lattice mismatch of $\gamma/\gamma'$,[3] element effects,[4] phase stability,[5] rafting,[6] creep curve prediction,[7] and microstructural simulation of creep deformation[8] in $\gamma/\gamma'$ hardening superalloys for gas turbine components. When used as a boiler material, however, ductility is as important as creep strength at high temperatures. In previous research, we observed microstructures with creep damage in a Ni-based alloy.[9] Then, we suggested that it is critical for the improvement of ductility to identify the creep failure mechanism.

In this study, the failure mechanism and classification of microstructural damage of Ni-based model alloys were used instead of the complex candidate materials[10] studied in A-USC projects. This research was conducted as part of fundamental research for achieving a creep rupture strength of 100 MPa at 1023 K (750 °C) and $10^5$ hours. Finally, we provide the creep rupture data of the alloys that were improved as a result of this study and establish that the alloy design guideline is reasonable.

## II. EXPERIMENTAL PROCEDURE

### A. Materials

Ni-based model alloys with a base composition of Ni-20 mass pct Cr-3 mass pct Mo were designed by Thermocalc ver. R with the TTNI6 database. Table I shows the composition of the alloys measured by inductively coupled plasma and the carbon measured by infrared absorption. Figure 1 shows the phase fractions of Ni-20 mass pct Cr-3 mass pct Mo-1.9 mass pct Ti-2 mass pct Al (Alloy A), as well as Ni-20 mass pct Cr-3 mass pct Mo-2 mass pct Al-1 mass pct Nb (Alloy B). Figure shows that the $\gamma'$-Ni$_3$(Al, Ti, Nb) phase is stable and the mole fractions of Alloys A and B are about 20 and 7 mol pct, respectively, at 1023 K (750 °C) in equilibrium.

Although the model alloys were designed to precipitate fine $\gamma'$ particles inside the grains and not at the grain boundaries, a small amount of Cr-rich phase, which was mostly M$_{23}$C$_6$ carbide (M = Cr, Mo) observed by electron diffraction and an electron probe microanalyzer, was found to precipitate along the grain boundary at an impurity of 0.002 mass pct C as shown

MITSUHARU YONEMURA, Senior Researcher, and HIROYUKI SEMBA, Chief Researcher, are with the Technical Research & Development Bureau, Nippon Steel & Sumitomo Metal Corporation, 1-8 Fuso-cho, Amagasaki, Hyogo 660-0891, Japan. Contact e-mail: yonemura.4k8.mitsuharu@jp.nssmc.com MASAAKI IGARASHI, Fellow, is with the Technical Research & Development Bureau, Nippon Steel & Sumitomo Metal Corporation, 20-1 Shintomi, Futtsu, Chiba 293-8511, Japan.

Table I.   Chemical Composition of the Designed Alloys

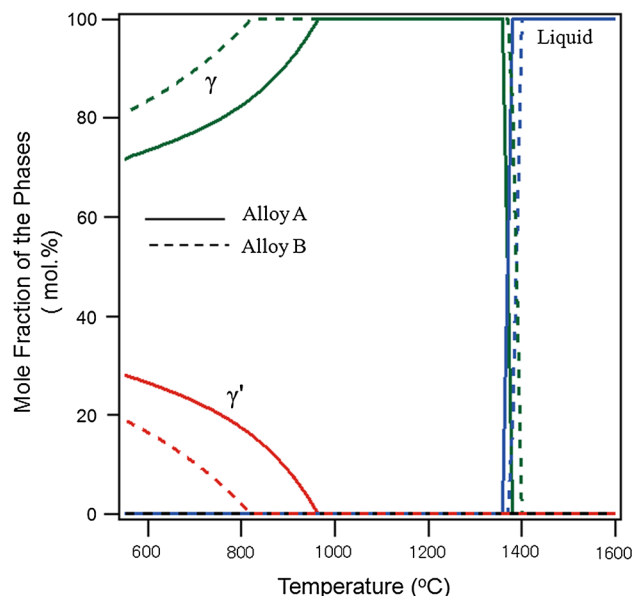| Alloy | Mass pct | | | | | | |
| | Ni | Cr | Mo | Al | Ti | Nb | C |
| --- | --- | --- | --- | --- | --- | --- | --- |
| A | bal. | 20.0 | 3.0 | 2.0 | 1.9 | — | 0.002 |
| B | bal. | 20.0 | 3.0 | 2.0 | — | 1.0 | 0.002 |
| C | bal. | 20.0 | 3.0 | 2.0 | 1.9 | — | 0.020 |



Fig. 1—Phase fractions of Ni-20 mass pct Cr-3 mass pct Mo-1.9 mass pct Ti-2 mass pct Al (Alloy A) are shown by the solid lines, and Ni-20 mass pct Cr-3 mass pct Mo-2 mass pct Al-1 mass pct Nb (Alloy B) are shown by the broken lines. The mole fractions of Alloy A and Alloy B are about 20 and 7 mol pct, respectively, at 1023 K (750 °C) in equilibrium.

in Table I, which will be explained later. Furthermore, Alloy C was created by adding 0.02 mass pct C to Alloy A. It was designed to investigate the influence of carbon, which forms many $M_{23}C_6$ carbides on the grain boundary, on the microstructure and creep properties.

B. *Specimen Preparation*

The model alloys were melted by vacuum induction and processed by hot forging into 40-mm-thick plates at 1403 K (1130 °C) and then hot rolling into 15-mm-thick plates at 1403 K (1130 °C). The plates were solution-heat-treated at 1323 K (1050 °C) for 1 hour followed by water-quenching and then aged at 1023 K (750 °C) for 32 hours. Following this, the crystal grain size of Alloys A, B, and C, which were measured by the average grain intercept method, were found to be 125, 100, and 120 $\mu$m, respectively. Although the target temperature for the test was 1023 K (750 °C), we also performed an accelerated test at 1123 K (850 °C). It should be noted that the initial stage of transition creep at 1123 K (850 °C) is a non-equilibrium process in which the creep rate is higher than coarsening rate of the

$\gamma'$ phase. Therefore, the initial microstructure in the accelerated test at 1123 K (850 °C) should include precipitation of enough $\gamma'$ phase and has an initial strength corresponding to 1023 K (750 °C). Then, the initial microstructures inside the grain are formed by the fine dispersion of $\gamma'$ particles with a spherical shape approximately 30 nm in diameter.

The high temperature accelerated test was performed at 1123 K (850 °C) with reference to the time–temperature–precipitation diagram of Nimonic263.[11] The creep time of $10^5$ hours at 1023 K (750 °C) was equivalent to that of approximately 600 hours at 1123 K (850 °C) according to the Larson–Miller parameter (LMP) conversions, using a constant of 20. Figure 2 shows the time dependence of area fraction (a) and size (b) of the $\gamma'$ particles at 1123 K (850 °C). Although it decreased from the initial heat-treated state at 1023 K (750 °C), the area fraction of $\gamma'$ phase was maintained during the time to rupture, which for all alloys was <700 hours at 1123 K (850 °C), and it was determined to be sufficient for the purpose of precipitation strengthening as shown in Figure 2(a). Furthermore, the coarse $\gamma'$ particles depended on the annealing time rather than the alloy composition as shown in Figure 2(b). Also, creep degradation has to be considered in conjunction with the kinetics of microstructure formation because the mole fraction decreases at an equilibrium temperature of 1123 K (850 °C). Therefore, creep deformation between 1023 and 1123 K (750 and 850 °C) will show the same mechanism as when the dislocation is pinned by a sufficient number of numerical $\gamma'$ particles, as explained later.

Figure 3 shows the creep rate–strain curve of Alloy A and C at a stress of 80 MPa and Alloy B at a stress of 50 MPa. The creep rate decreased rapidly with creep strain in the transient creep. Alloy A ruptured at 646 hours with a rupture elongation of about 7 pct. To observe the microstructure of the creep degradation, the creep test was interrupted at 1, 144, and 504 hours, which corresponds to the transient creep, minimum creep rate, and accelerated creep, respectively. In contrast, Alloy B ruptured at 455 hours with a rupture elongation of about 50 pct. Similarly, the creep test was interrupted at 1, 45, 215, and 400 hours, which corresponds to the transient creep, minimum creep rate, and two accelerated creeps, respectively. Alloy B, which was designed with a smaller mole fraction of the $\gamma'$ phase, exhibited a higher minimum creep rate and higher rupture elongation than Alloy A. Furthermore, Alloy C ruptured at 2045 hours with a rupture elongation of about 16 pct.

The microstructures were observed using scanning electron microscopy (SEM) and transmission electron
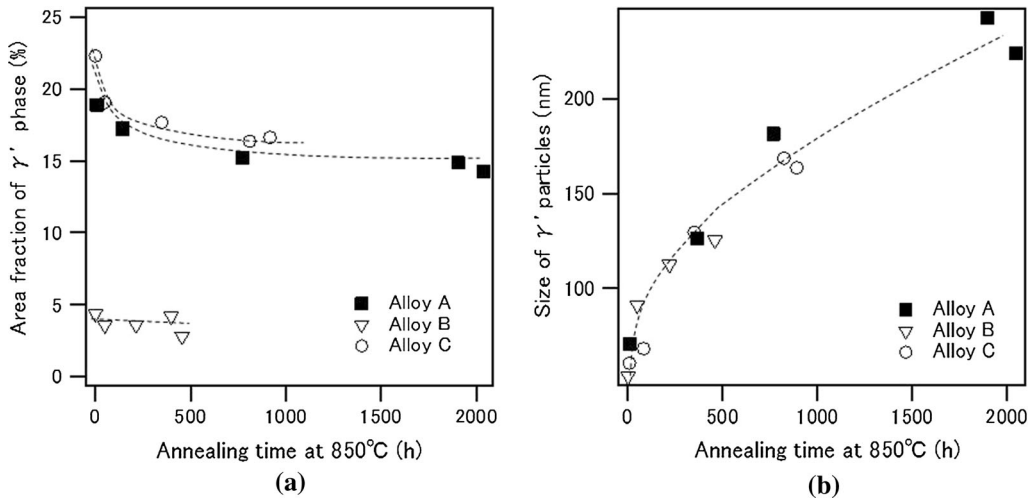
Fig. 2—Time dependence of the area fraction (*a*) and size (*b*) of the $\gamma'$ particles at 1123 K (850 °C). Although it decreases from the initial heat-treated state at 1023 K (750 °C), the area fraction of $\gamma'$ phase is maintained during the time to rupture, which for all alloys was <700 h at 1123 K (850 °C), and it is sufficient for the purpose of precipitation strengthening as shown in (a). Furthermore, the coarsening of $\gamma'$ particles depends on annealing time rather than the alloy composition as shown in (b).
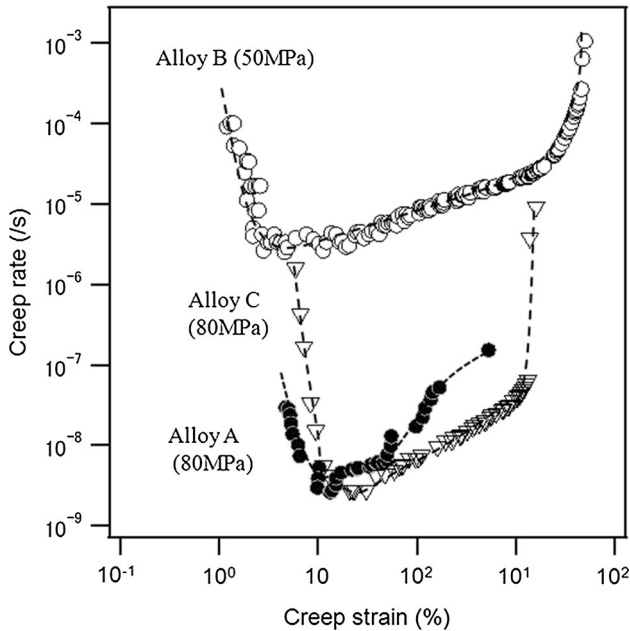


Fig. 3—Creep curve of Alloys A, B, and C at 1123 K (850 °C). Alloy A and Alloy C, which have a larger mole fraction of $\gamma'$ phase, show higher strength and lower ductility than Alloy B. The interruptions were conducted at the transient creep, minimum creep rate, and accelerated creep to observe the creep degradation and make a comparison between the microstructures of Alloy A and Alloy B.

microscopy (TEM). The SEM characterization was performed using a HITACHI microscope with a field-emission gun operated at 15 kV. The TEM characterization was performed using a Tecnai transmission electron microscope operated at 300 kV. The TEM specimens were prepared using the ion-milling and the focused ion beam method (FIB) for the accelerated creep and ruptured specimens.

## III. RESULTS AND DISCUSSION

### A. *Microstructure of High-Strength Ni-Based Model Alloys*

Figures 4(a) through (c) shows the SEM micrographs of microstructures at the transient creep, minimum creep rate, and accelerated creep of Alloy A. The particle size is the average size of 50 $\gamma'$ particles, which were removed by an extraction replica method. It was confirmed that the size of the $\gamma'$ particles inside grains increased to about 100 nm at the transient creep, 180 nm during the minimum creep rate, and 220 nm at the accelerated creep with creep deformation. In the model alloy, most of the $\gamma'$ phase precipitates were nearly spherical with the exception of some of the particles at the grain boundaries in a few of the presented conditions, as shown in Figure 4. The $\gamma'$ particles inside the grains tended to align with the creep time. This behavior is due to the elastic strain between the $\gamma$ matrix and $\gamma'$ particles and the elastic interactions between adjacent $\gamma'$ particles.[12] In the proximity of grain boundaries, the coarse $M_{23}C_6$ resulting from carbon impurities was locally observed along the grain boundaries during transient creep. Subsequently, the $\gamma'$ particles agglomerated into a massive form on the grain boundary at the minimum creep rate, as shown in Figure 4(b). Finally, the $\gamma'$ particles deformed to form nodules during the accelerated creep, as shown in Figure 4(c). Then, a precipitate-free zone (PFZ) formed in the proximity of the grain boundaries. It is expected that the formation of nodule-like $\gamma'$ phases is associated with the grain boundary migration during accelerated creep, as will be discussed later. Thus, the microstructure around the grain boundaries was altered remarkably, while the $\gamma'$ particle size increased linearly inside the grains. Furthermore, the microstructures during creep deformation were observed by TEM, as shown in Figures 4(d) through (f). During transient creep, the dislocations
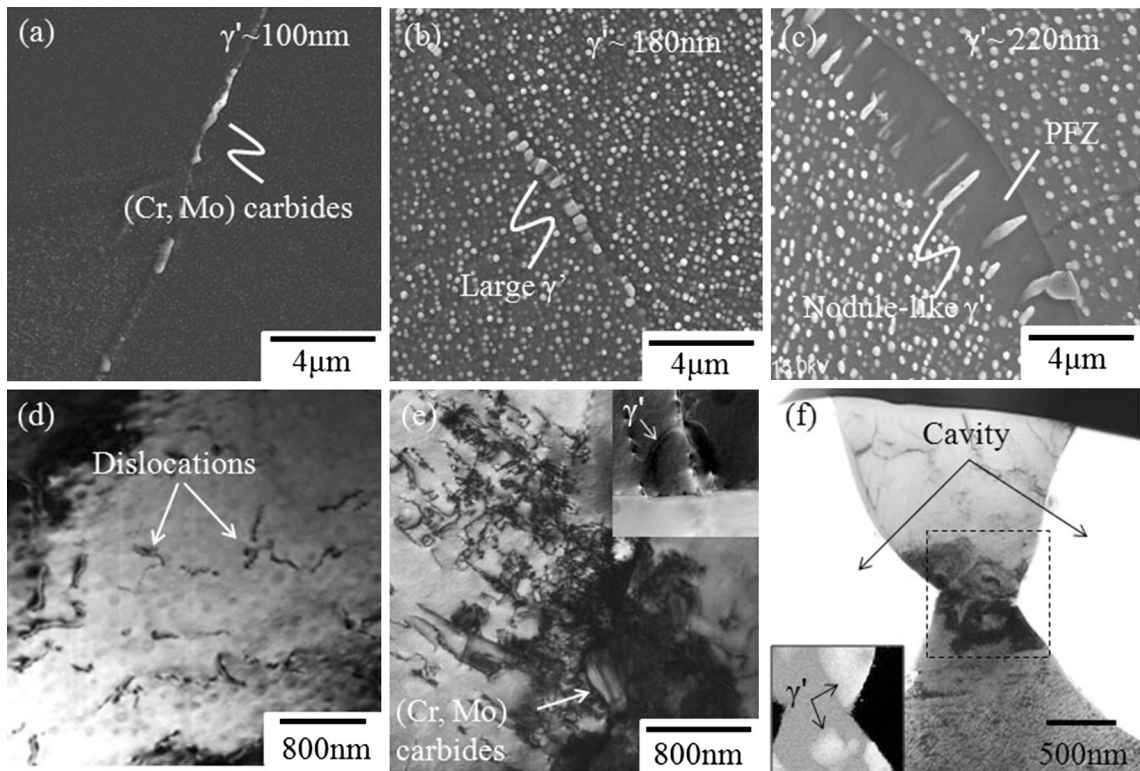
Fig. 4—SEM and TEM micrographs of the microstructures at transient creep (*a, d*), minimum creep rate (*b, e*), and accelerated creep (*c, f*). The upper and lower images show SEM and TEM micrographs, respectively. The SEM micrographs show a coarsening of the γ' inside the grain (b, c), the formation of coarse γ' particles (b), and PFZ and nodule-like γ' phase (c) on the grain boundary during creep. The TEM micrographs show the accumulation (d) and multiplication (e) of dislocations and the initiation of cavities in PFZ (f). The inset image shows Ni mapping of the dashed line frame in (f).
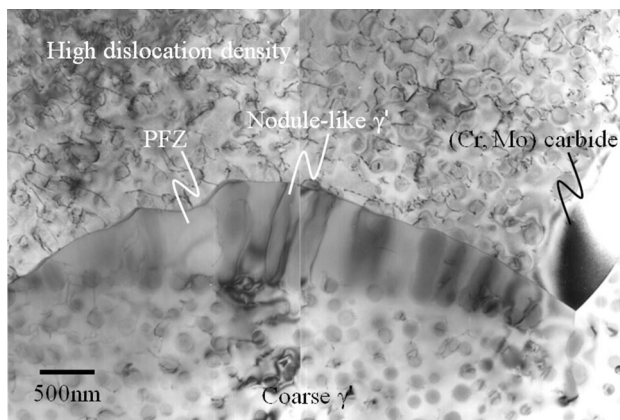


Fig. 5—TEM micrograph of microstructural damage in Alloy A at the minimum creep rate. Nodule-like γ' phase and PFZ are observed with a bowing of the grain boundaries toward the grain with a high dislocation density at the grain boundaries without coarse precipitates.

multiplied inside the grains with creep deformation, as shown in Figure 4(d). At the minimum creep rate, the cuboidal γ' particles inside the grains aligned along ⟨001⟩$_\gamma$, although the spherical particles were more randomly distributed inside the grains during transient creep. At the minimum creep rate, the dislocations accumulated at the grain boundaries with precipitates, as shown in Figure 4(e), although few of the grain boundaries had precipitates in Alloy A. The dislocation was localized extensively around the grain boundary. Dislocation bypassing seems to be Orowan looping inside the grain. However, some γ' particles on the grain boundaries were sheared by dislocation. In contrast, nodule-like γ' phases and PFZ were observed with a bowing of the grain boundaries toward the grain with a high dislocation density at the grain boundaries without coarse precipitates, as shown in Figure 5. In other words, the precipitation on the grain boundary controls the grain boundary migration and formation of PFZ. It is considered that this local stress concentration is a factor in cavitation. During accelerated creep, cavities were observed near the grain boundaries, as shown in Figure 4(f). The insert shows Ni mapping of the dashed line frame. The cavities initiated in the PFZ, which has low-creep strength. Furthermore, coarse γ' particles were distributed sparsely in the constricted microstructure, as evidenced by electron diffraction and element mapping, although this feature was not distinguishable in the bright-field images. It is considered that the γ' particles are an obstacle to destruction, as a constriction occurs along the coarse γ' particles. Therefore, the precipitates at the grain boundaries, such as coarse γ' particles, suppress the coalescence of cavities. This is a key factor governing creep degradation. Based on these results, the local stress concentration at the grain
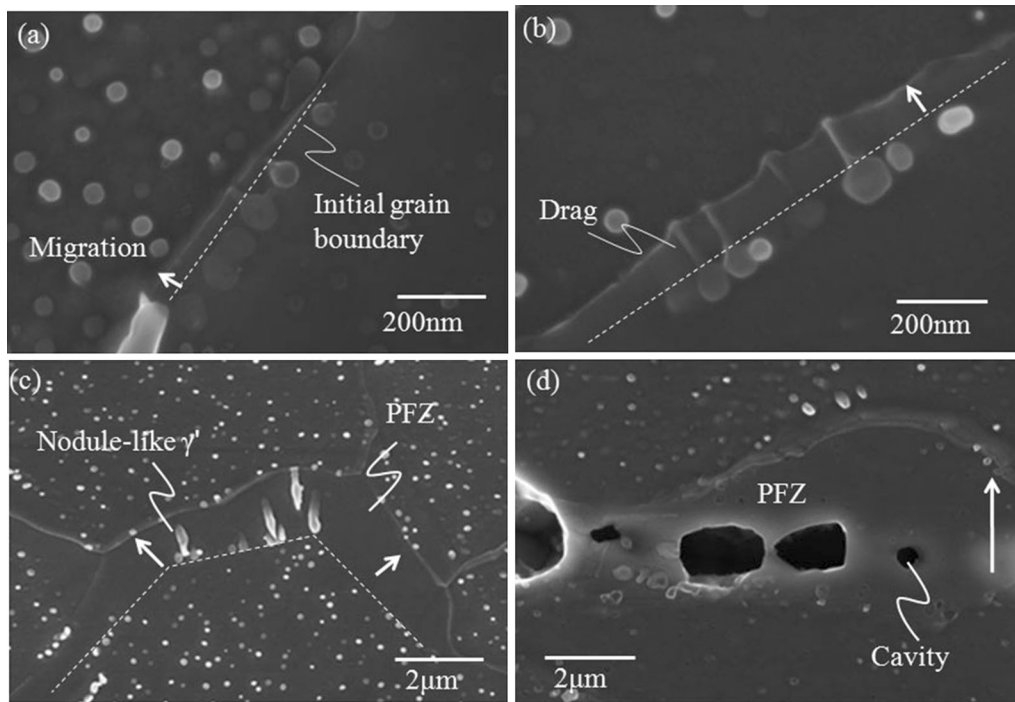
Fig. 6—SEM micrographs of the microstructure of Alloy B at the transient creep (*a*), minimum creep rate (*b*), and accelerated creep (*c*, *d*). The broken line shows the initial grain boundary. The grain boundary migrates with the dragging of γ′. Then, nodule-like γ′ and PFZ form, and cavities initiate in the PFZ.

boundaries and formation of PFZs are major causes of creep degradation. It should be noted that the creep strength can be improved by suppressing the formation of PFZ.

## B. *Microstructure of High-Ductility Ni-Based Model Alloys*

The microstructure of high-ductility, low-strength Alloy B was observed to show clear grain boundary deformation. Alloy B was subjected to a creep test, and the test was interrupted during the accelerated creep, at which point the creep elongation was 34 pct after being subjected to a stress of 50 MPa at 1123 K (850 °C) for 400 hours. With the high density of γ′ particles inside the grain in Alloy A, as shown in Figure 6, the γ′ particles appeared to form nodules at the grain boundaries. Even though the density of the γ′ phase inside the grain was low, the crystal growths of γ′ particles extended to the grain with a high dislocation density as if they were dragged by the grain boundary during the transient creep and minimum creep rate, as shown by the arrows in Figures 6(a) and (b). Here, the initial location of the grain boundaries was assumed to be a linear boundary with the same crystal orientation as the grain boundary with different crystal orientation bows during creep. During accelerated creep, the formation of nodule-like γ′ particles from the initial grain boundaries and PFZs was observed locally and sparsely, as shown in Figure 6(c). Cavities formed in the large PFZ, where the creep strength was weaker than other areas, as shown in Figure 6(d). Furthermore, the formation of PFZ was associated with the bowing of the grain boundaries. This

bowing suggests the presence of strain-induced grain boundary migration (SIBM). In general, the grain boundary migration follows the atomic diffusion across the boundaries. The precipitates behave as pinning sites of migration or dissolve if their size is less than or equal to the critical size.[13] In this study, the initial grain boundary was locally decorated by coarse $M_{23}C_6$ and coarse γ′ phase. This indicates that coherent γ′ phases dissolved with SIBM, whereas the coarse $M_{23}C_6$ led to the pinning of SIBM. Furthermore, γ′ phases tended to grow on the γ′ particles along the initial grain boundaries or the nucleation of γ′ phases occurred due to oversaturation on the SIBM. In other words, SIBM tended to exhibit nodule-like growth due to the diffusion of γ′ stabilization elements such as Al, Ti, and Nb, which is similar to Ostwald ripening. Consequently, the microstructure around the grain boundaries was altered remarkably by SIBM, while the γ′ particle size increased linearly inside the grains with increasing temperature and time.

Figure 7 shows a TEM micrograph of a PFZ and an annular dark-field scanning transmission electron microscopy (ADF-STEM) image of the dislocation network. The PFZ was identified to be SIBM since it is well-known that grain boundaries migrate from a low dislocation density grain to a high dislocation density grain. The area surrounded by the dashed line corresponds to the PFZ. Furthermore, coarse γ′ phases were observed along the interface of the PFZ/matrix. Dahlén *et al.* reported that the primary γ′-precipitate dispersion dissolves at the migrating recrystallization front and reprecipitates discontinuously in the recrystallization grain.[14] Furthermore, Porter et al. reported that high
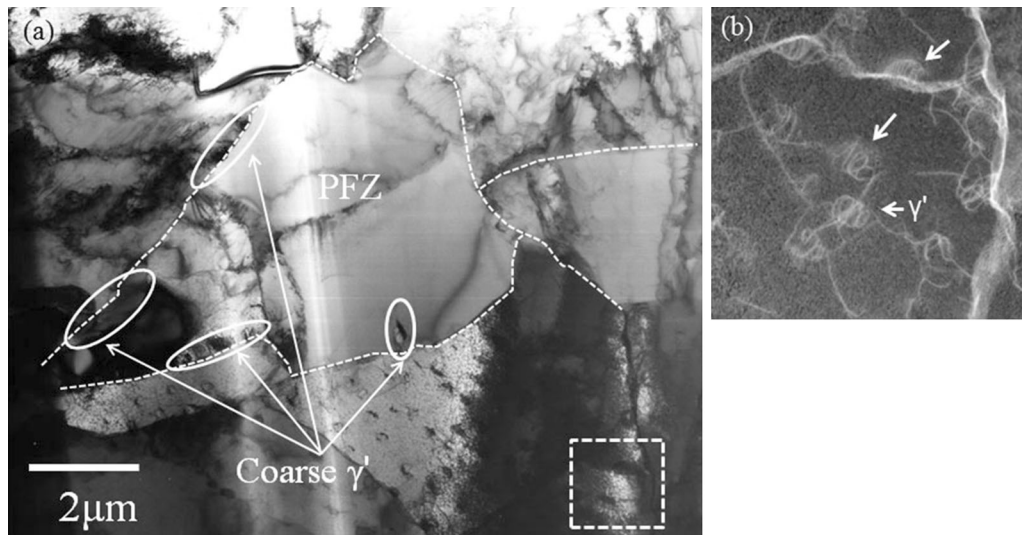
Fig. 7—TEM micrograph of a PFZ with coarse $\gamma'$ particles at the grain boundary (*a*) and ADF-STEM image of dislocation networks (*b*) in Alloy B. The broken lines show the PFZ. (b) shows an enlarged view of the dashed line frame in (a). The arrows show the interaction between $\gamma'$ and dislocations.
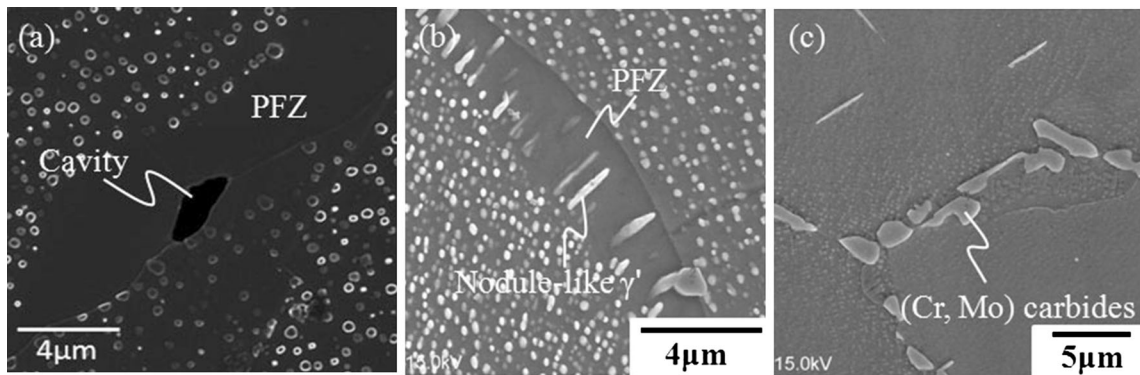


Fig. 8—Classification of microstructural damage. They are low-density $\gamma'$ particles inside the grains and precipitation free at grain boundaries such as in Alloy B (*a*), high-density $\gamma'$ particles inside the grains and precipitation free at grain boundaries such as in Alloy A (*b*), and high-density $\gamma'$ particles inside the grains and precipitations at the grain boundaries such as in Alloy C (*c*). The size of the PFZ varies depending on the mole fraction of $\gamma'$ and grain boundary coverage. The PFZ decreases as the volume fraction of $\gamma'$ and grain boundary coverage increases, thus improving creep strength.

diffusivity assumes greater importance as the amount of solute dissolved in the boundary increases. Growth of the nucleus occurs by strain-induced boundary migration.[15]

Therefore, it is suggested that the small $\gamma'$ particles dissolve on the SIBM, and subsequently, these $\gamma'$ particles precipitate and become coarser along the grain boundaries when the dissolved $\gamma'$ stabilization elements oversaturate on the grain boundaries. Then, SIBM is pinned by the precipitated $\gamma'$ particles at the grain boundaries. Moreover, the interactions between the $\gamma'$ particles, dislocations, and dense dislocation walls were observed inside the grains by ADF-STEM, as shown in Figure 7(b). The $\gamma'$ particles inside the grains pinned the dislocations even during accelerated creep.

### C. Classification of the Damaged Microstructures

Figure 8 shows the detailed microstructures at the grain boundaries after creep. The microstructures are classified based on the absence or presence of precipitation at the grain boundaries. Furthermore, they are divided into low or high density based on the concentration of $\gamma'$ particles inside the grains. The volume fraction of the $\gamma'$ phase is strongly correlated with PFZ size in the case of the microstructure with precipitate-free grain boundaries, such as Alloy B shown in Figure 8(a). Also, the cuboidal $\gamma'$ particles deform to form nodules during grain boundary migration in the case of a high density of $\gamma'$ particles. This phenomena depends on the dissolution and growth of $\gamma'$ particles. On the other hand, large PFZ form because of grain boundary migration in the case of a low density of $\gamma'$ particles, such as Alloy A shown in Figure 8(b). The dissolution of a small amount of $\gamma'$ particles does not provide enough oversaturation for re-precipitation of the $\gamma'$ phase. In other words, numerous precipitates along the grain boundaries pin the grain boundary migration. Furthermore, the precipitates along the grain boundaries suppress the formation of PFZ, such as in

Alloy C shown in Figure 8(c). Coarse precipitates such as $M_{23}C_6$ pin the SBIM, whereas the fine precipitates such as $\gamma'$ particles dissolve with SBIM. Therefore, the volume fraction of the $\gamma'$ phase and amount of precipitation on the grain boundary, (i.e., proportion of the grain boundary covered by precipitates) are associated with the size of the PFZ, which is a major factor in creep damage. Furthermore, appropriate precipitation inside the grains and at the grain boundaries is very effective for suppressing PFZ. Numerous studies have been conducted on PFZ.[16–18] These studies discuss the improvement of strength and ductility by controlling PFZ. PFZs are usually associated with grain boundary precipitates. In the case of austenitic steels, chromium-containing precipitates like $Cr_{23}C_6$ are thought to play an important role by lowering the solubility of $\gamma'$-forming elements. Wang et al. found that carbides prevent the migration of recrystallized grain boundaries through various pinning mechanisms.[19] In contrast, our study is related to time-dependent crystal growth, such as the formation of nodule-like $\gamma'$ phase during dynamic grain boundary migration. In the case of high temperature creep in austenitic steel, crystal grain size in excess of approximately 100 $\mu$m has little effect on the creep properties.[20] The three alloys in this study have an initial grain size of about 100 to 125 $\mu$m. Therefore, it is considered that the formation of PFZ influences the grain boundary coverage and the mass fraction of the $\gamma'$ phase inside grain without dependence on the crystal grain size. In addition, the difference between the crystal grain sizes in these alloys does not greatly influence grain boundary migration since the driving force of grain boundary migration is the difference in dislocation density. However, the relationship between grain boundary coverage and crystal grain size must be investigated in detail from the viewpoint of microstructure control.

As mentioned above, the study of creep degradation in model alloys provides important information about complex candidate alloys for A-USC power plants. In addition, creep failure in model alloys is also expected to occur in complex systems. As shown in Figure 9, the strength level of the developed alloy was estimated from the stress vs LMP curve obtained at 1023 K (750 °C) and accelerated testing at 1123 K (850 °C). The LMP converts 1023 K (750 °C) $\times$ $10^5$ hours to 25.58 using a constant of 20. First, Alloy B is strengthened by a small number of $\gamma'$ particles inside the grain. Therefore, it has low strength and high ductility since the grain deforms easily, as shown by the rupture elongation ($\varepsilon_r$) of 50 pct at a stress of 130 MPa. In other words, because Alloy B has a small amount of the $\gamma'$ particles in the matrix, it has the highest ductility resulting mainly from the ease at which the crystal grain deforms. Furthermore, cavities are easily formed in the PFZ since the largest PFZ is formed by the grain migration in the precipitation-free grain boundary.

By increasing the mole fraction of the $\gamma'$ phase, the creep strength improves to a level similar to Alloy A, as shown by the broken line with a triangle symbol in
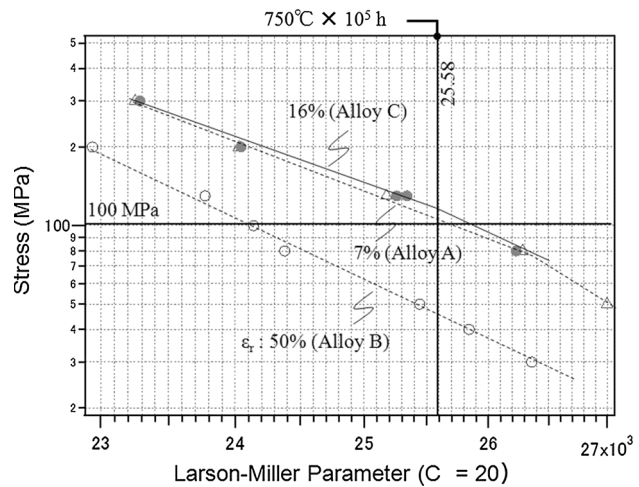


Fig. 9—Creep rupture data of Ni-based model alloys as a function of the Larson–Miller parameter. $\varepsilon_r$ shows the rupture elongation at a stress of 130 MPa. Alloy A, B, and C at 130 MPa correspond to the microstructures in (b), (a), and (c), respectively.

Figure 9. However, this improvement in creep strength is accompanied by a loss of ductility until $\varepsilon_r$ = 7 pct. Although the addition of Nb in Alloy B can improve the ductility,[21,22] the large decrease in elongation in Alloy A is considered to be related to the microstructure. That is, grain boundary deformation is dominant since it is difficult for grains with a high density of $\gamma'$ to deform. The ductility is improved by precipitations, such as carbides, at the grain boundaries. Such a high-strength, high-ductility alloy was created as Alloy C, which has 0.02 mass pct C added to Alloy A since the precipitates on the grain boundaries suppress the formation of PFZ, as shown in Figure 8(c). The precipitation of $M_{23}C_6$ particles by the addition of carbon suppresses the grain boundary migration and formation of PFZ. Suppression of the grain boundary migration is correlated with the strength of the grain boundary. The balance between the grain boundary strength and the grain strengthened by $\gamma'$ particles improves the elongation. Furthermore, a small amount of PFZ improves the elongation by suppressing the formation of cavities. Based on this, higher creep ductility is caused by a combination of an appropriate hard matrix resulting from fine dispersion of the $\gamma'$ phase and a grain boundary with precipitates.

As mentioned above, the most important point is to suppress the formation of PFZ near the grain boundaries. Here, coarse precipitate covered grain boundaries accumulate considerable dislocations. In contrast, precipitate-free grain boundaries form PFZ with low-creep strength. Both phenomena induce microstructural damage. Therefore, the creep properties are improved by controlling PFZ in proximity to the grain boundaries for a superior balance of creep strength and ductility. In addition, the creep strength inside the grains should be controlled by a suitable fraction of $\gamma'$ phases. Consequently, we designed an alloy with high-creep strength and high ductility based on the microstructure

degradation analysis and obtained a reasonable alloy design guideline.

## IV. CONCLUSION

The creep degradation of Ni-based model alloys was studied, and the following results were obtained: (i) The microstructure around grain boundaries is altered remarkably by SIBM, while the $\gamma'$ particle size increases linearly inside the grains with increasing temperature and time. (ii) The volume fraction of the $\gamma'$ phase and proportion of the grain boundary covered by precipitates are correlated with the size of the PFZ, which is a major factor in creep damage. (iii) Appropriate precipitation inside the grains and at the grain boundaries is very effective for suppressing PFZ. (iv) The creep properties are improved by controlling PFZ located near the grain boundaries for a superior balance between creep strength and ductility.

We designed and prototyped high-creep-strength alloys under 100 MPa at 1023 K (750 °C) for $10^5$ hours. The alloys showed high ductility with a rupture elongation of more than 50 pct resulting from a decrease in PFZ and controlling the SBIM through precipitation on the grain boundary.

## REFERENCES

1. M. Yonemura, T. Hamaguchi, H. Semba, and M. Igarashi: *First Symposium for Project on Fundamental Studies on Technology for Enhanced Strength and Functions*, New energy and industrial technology development organization. 2009, pp. 77–78.
2. M. Doi: *Prog Mater. Sci.*, 1996, vol. 40, p. 79.
3. H.-A. Kuhn, H. Biermann, T. Ungár, and H. Mughrabi: *Acta Metall. Mater.*, 1991, vol. 39, pp. 2783–94.
4. M. Enomoto and H. Harada: *Metall. Trans. A*, 1989, vol. 20A, pp. 649–64.
5. J.-C. Zhao, V. Ravkumar, and A.M. Beltran: *Metall. Mater. Trans.*, 2001, vol. 32A, pp. 1271–82.
6. T.M. Pollock and A.S. Argon: *Acta Metall. Mater.*, 1994, vol. 42, pp. 1859–74.
7. B.F. Dyson and T.B. Gibbons: *Acta Metall.*, 1987, vol. 35, pp. 2355–69.
8. Y. Tsukada, Y. Murata, T. Koyama, N. Miura, and Y. Kondo: *Acta Mater.*, 2011, vol. 59, pp. 6378–86.
9. M. Yonemura, T. Hamaguchi, H. Semba, and M. Igarashi: *12th Inter. Conf. Creep and Fracture of Engineering Materials and Structures*. 2012, pp. A45.
10. X. Xie, S. Zhao, and J. Dong: *5th Inter. Conf. Adv. in Materials Technology for Fossil Power Plants*, Electric Power Research Institute. 2007, pp. 3A–6.
11. A.J. Ardell, R.B. Nicholson, and J.D. Eshelby: *Acta Metall.*, 1966, vol. 15, pp. 1295–1309.
12. J.Z. Zhua, T. Wanga, A.J. Ardellb, S.H. Zhoua, Z.K. Liua, and L.Q. Chena: *Acta Mater.*, 2004, vol. 52, pp. 2837–45.
13. R.D. Doherty: *Met. Sci.*, 1982, vol. 16, pp. 1–14.
14. M. Dahlén and L. Winberg: *Acta Metall.*, 1980, vol. 28, pp. 41–50.
15. A. Porter and B. Ralph: *J. Mater. Sci.*, 1981, vol. 16, pp. 707–13.
16. G.S. Was: *Corrosion*, 1990, vol. 46, pp. 319–30.
17. T. Ogura, S. Hirosawa, and T. Sato: *Mater. Sci. Forum*, 2007, vols. 561–565, pp. 235–38.
18. Y.L. Chiu and A.H.W. Ngan: *Metall. Mater. Trans.*, 2000, vol. 31A, pp. 3179–86.
19. L. Wang, G. Xie, J. Zhang, and L.H. Lou: *Scripta Mater.*, 2006, vol. 55, pp. 457–60.
20. T. Terada, T. Matsuo, and M. Kikuchi: in *Aspects of High Temperature Deformation and Fracture*, Y. Hosoi, ed., The Japan Institute of Metals and Materials, 1993, p. 27.
21. M. Yonemura, T. Hamaguchi, H. Semba, and M. Igarashi: *CAMP-ISIJ*, 2008, vol. 21, p. 1349.
22. T.B. Gibbons and B.E. Hopkins: *Met. Sci. J.*, 1971, vol. 5, p. 233.